RSC Advances

PAPER

View Article Online
View Journal | View Issue

Cite this: *RSC Adv.*, 2017, **7**, 39082

Computational assisted design of the favored composition for metallic glass formation in a Ca–Mg–Cu system

S. Zhao, J. H. Li,* S. M. An, S. N. Li and B. X. Liu

To well predict the favored composition for metallic glass formation in a Ca–Mg–Cu system, a realistic interatomic potential was first constructed for the system and then applied to Monte Carlo simulations. The simulation not only predicts a hexagonal composition region for metallic glass formation, but also provides a favored sub-region within which the amorphization driving force is larger than that outside. The simulations show that the physical origin of glass formation is the solid solution collapsing when the solute atom exceeds the critical solid solubility. Further structural analysis indicates that the 1551 bond pairs (icosahedral-like) dominate in the favored sub-region. The large atomic size difference between Ca, Mg, and Cu extends the short-range landscape, and a microscopic image of the medium-range packing can be described as an extended network of pentagonal bipyramids entangled with four-fold and six-fold disclinations, together fulfilling the space of the metallic glasses. The predictions are well supported by the experimental observations reported to date and can provide guidance for the design of ternary glasses.

Received 19th May 2017
Accepted 25th July 2017

DOI: 10.1039/c7ra05650h

rsc.li/rsc-advances

I. Introduction

Bulk metallic glasses (BMGs) have attracted extensive attention since their first discovery.[1–3] BMGs possess various unique properties such as high yield strength, hardness, corrosion resistance, and elastic strain limit,[4–7] which make the BMGs a promising material for a wide range of applications. Although BMGs have been investigated for several decades, some basic issues, for example the prediction of the glass forming range (GFR) and glass forming ability (GFA), have not been satisfyingly clarified. Previous criteria of characterizing the GFR and GFA include the deep eutectic,[8] size difference,[9] structural difference[10] rules, and others.[11–13] These rules belong to the empirical/semi-empirical rules, and the predictions are not satisfactory enough. Thus, it is necessary to propose a starting base to predict the glass formation, which reflects the internal characteristics of the system. As has been reported,[10] the GFA can be considered as intrinsic characteristics of a given system and should be governed by internal atomic interactions, which can be described by its interatomic potential. Therefore, it is feasible to take the interatomic potential as the basis to clarify the underlying physics of glass formation and predict the favored glass formation compositions for a given system.

Previous research has indicated that Ca–Mg-based[14–16] glasses have properties, such as very low Young's and shear moduli,[17] low density,[18] and strong relaxation dynamics of the super-cooled liquid,[19] that distinguish them from transition-metal-based bulk metallic glasses. It has been reported that ternary Ca–Mg–Cu systems have a good GFA with the maximum diameters of up to 9 mm and 10 mm obtained in $Ca_{50}Mg_{25}Cu_{25}$ and $Ca_{50}Mg_{22.5}Cu_{27.5}$, respectively.[15] Moreover, the large difference in the distribution of their atomic radii (Ca (1.9 Å), Mg (1.6 Å), and Cu (1.25 Å)) makes the separation of the partial distribution functions relatively easy and unambiguous. Thus, this triggered our interest to carry out a comprehensive investigation on glass formation in the Ca–Mg–Cu system based on an atomistic approach.

II. Ca–Mg–Cu interatomic potential

The interatomic potential is of critical importance to atomistic simulations[10] since it intrinsically governs and reasonably describes the various physical and chemical properties of a specific system. In this study, the atomic potential of the Ca–Mg–Cu system was constructed under the framework of long-range second-moment-approximation of tight-binding (TB-SMA),[20,21] which can be written as follows:

$$E_i = \frac{1}{2}\sum_{j\neq i}\varphi(r_{ij}) - \sqrt{\sum_{j\neq i}\psi(r_{ij})} \quad (1)$$

$$\varphi(r_{ij}) = \begin{cases} 2A_1 \exp\left[-p_1\left(\frac{r_{ij}}{r_0}-1\right)\right], & r_{ij} \le r_{m1} \\ 2A_{1m} \exp\left[-p_{1m}\left(\frac{r_{ij}}{r_0}-1\right)\right]\left(\frac{r_{c1}}{r_0}-\frac{r_{ij}}{r_0}\right)^{n_1}, & r_{m1} < r_{ij} \le r_{c1} \end{cases} \quad (2)$$

Key Laboratory of Advanced Materials (MOE), School of Materials Science and Engineering, Tsinghua University, Beijing 100084, China. E-mail: lijiahao@mail.tsinghua.edu.cn

$$\psi(r_{ij}) = \begin{cases} A_2 \exp\left[-p_2\left(\frac{r_{ij}}{r_0}-1\right)\right], & r_{ij} \le r_{m2} \\ A_{2m} \exp\left[-p_{2m}\left(\frac{r_{ij}}{r_0}-1\right)\right]\left(\frac{r_{c2}}{r_0}-\frac{r_{ij}}{r_0}\right)^{n_2}, & r_{m2} < r_{ij} \le r_{c2} \end{cases} \quad (3)$$

where E_i is the total potential energy of atom i, φ and ψ are the pair and density items, respectively, and r_{ij} is the distance between the atom i and j. $p_1, A_1, r_{m1}, A_{1m}, r_{c1}, p_{1m}, p_2, A_2, r_{m2}, A_{2m}$, r_{c2}, and p_{2m} are the potential parameters to be determined, and n_1 and n_2 are set as 4 and 5, respectively. More details of the relevant parameters can be found in the literature.[20] Based on this formula, it can be deduced that the pair item and density items, as well as their first derivatives, smoothly approach zero at the cut-off distance; this avoids some non-physical behaviors.[22]

In the Ca–Mg–Cu system, six sets of potential parameters, *i.e.*, Ca–Ca, Mg–Mg, Cu–Cu, Ca–Mg, Ca–Cu, and Mg–Cu, should be fitted. These potential parameters are fitted to the referenced physical properties of the elements or compounds. Specifically, the parameters of Ca–Ca, Mg–Mg, and Cu–Cu are determined by fitting them to the physical properties, such as lattice constant, cohesive energy, elastic constant, and bulk modulus, of Ca, Mg, and Cu. The parameters of the Ca–Mg, Ca–Cu, and Mg–Cu cross potentials are determined by fitting them to the properties of the stable or virtual intermetallic compounds in each binary system. In the fitting, *ab initio* calculations using the Cambridge Serial Total Energy Package (CASTEP)[23] were applied to calculate the relevant properties of the compounds. The six fitted potential parameters of the system are listed in Table 1. Tables 2 and 3 provide the cohesion energies, elastic constants, and bulk moduli of Ca, Mg, and Cu and their compounds obtained by fitting experiments or *ab initio* calculations.[24,25] It is clearly seen that the physical properties reproduced by the parameters, experimental results, or *ab initio* calculations are all in good accordance; this indicates that the constructed Ca–Mg–Cu interatomic potential can describe the energetic and structural characteristics in the system.

Table 2 Lattice constants (a and c), cohesive energies E_c, elastic constants C_{ij}, and bulk moduli B_0 of Ca, Mg and Cu fitted by the potential and obtained from experimental data or *ab initio* calculations

	fcc-Ca		hcp-Mg[a]		fcc-Cu[a]	
	Fitted	*ab*	Fitted	exp	Fitted	exp
a (Å)	5.521	5.521	3.209	3.209	3.611	3.615
c (Å)			5.235	5.21		
E_c (eV)	1.839	1.840	1.508	1.510	3.502	3.490
C_{11} (Mbar)	0.219	0.186	0.591	0.595	1.688	1.683
C_{12} (Mbar)	0.149	0.157	0.270	0.261	1.225	1.221
C_{13} (Mbar)			0.223	0.218		
C_{33} (Mbar)			0.642	0.616		
C_{44} (Mbar)	0.143	0.088	0.112	0.164	0.745	0.757
B_0 (Mbar)	0.168	0.167	0.362	0.354	1.361	1.370

[a] Ref. 47.

Moreover, we have compared the equation of state (EOS) derived from the potential with the Rose equation[26] to determine whether the potential can describe the atomic interactions under the non-equilibrium state. Fig. 1 shows the pair terms, n-body parts, and total energies reproduced from the potential together with the corresponding Rose equations for Ca, Mg, Cu, Ca_2Mg, $CaCu_3$, and Mg_2Cu. It can be seen that they are all continuous and smooth over the entire range. Moreover, the EOSs derived from the proposed potential agree well with the corresponding Rose equations. This suggests that the constructed Ca–Mg–Cu potential can be applied to describe the atomic interactions even if the system is far from the equilibrium state.

III. Simulation models and characterization methods

As is reported,[10,27–29] the process of glass production is always non-equilibrium such that kinetic conditions are always limited and complicated intermetallic compounds are not able to

Table 1 The fitted potential parameters of the Ca–Mg–Cu system

	Ca	Mg[a]	Cu[a]	Ca–Mg	Ca–Cu	Mg–Cu
p_1	9.780032	10.37307	11.08757	9.118697	7.373268	9.671258
A_1 (eV)	0.165598	0.145780	0.287580	0.246665	0.480305	0.195924
r_{m1} (Å)	3.715213	3.522308	1.976092	2.967012	3.049149	3.066932
n_1	4	4	4	4	4	4
p_{1m}	3.413309	3.850843	4.485833	4.019030	2.268648	2.350010
A_{1m} (eV)	1.446073	0.538535	8.372519	1.442270	1.692311	1.361933
r_{c1} (Å)	6.167967	5.487015	3.486092	5.723657	6.069455	4.639665
p_2	4.814647	4.375061	3.669412	4.380322	4.356266	4.365612
A_2 (eV^2)	1.232266	0.951887	4.991288	1.490516	5.277673	2.498548
r_{m2} (Å)	3.908279	2.588516	2.803510	3.008102	4.406548	3.180829
n_2	5	5	5	5	5	5
p_{2m}	0.000389	0.000378	0.000695	0.000389	0.000685	0.000381
A_{2m} (eV^2)	1.014402	1.130393	0.671240	1.445114	0.243946	0.801356
r_{c2} (Å)	7.962903	6.250000	6.200000	7.020141	7.937850	6.478011
r_0 (Å)	3.904000	3.203567	2.492155	3.514492	3.228800	2.878592

[a] Ref. 47.

Table 3 The properties reproduced from the interatomic potential (first line) and calculated *via ab initio* methods for Ca–Mg, Ca–Cu, and Mg–Cu compounds[a]

Compounds	Space group	a or a, c or a, b, c (Å)	E_c (eV)	B_0 (Mbar)
Ca_2Mg	$I\bar{4}mmm$	4.033, 13.785	1.790	0.237
		3.943, 13.547	1.789	0.217
CaMg	$Pm\bar{3}m$	4.099	1.766	0.261
		3.970	1.768	0.248
$CaMg_2$	$P6_3/mmc$	6.334, 10.310	1.746	0.309
		6.245, 10.112	1.746	0.285
$CaCu_3$	$Pm\bar{3}m$	4.127	2.926	0.663
		4.059	2.927	0.728
CaCu	$Pm\bar{3}m$	3.555	2.722	0.468
		3.561	2.726	0.401
Ca_2Cu	$Pnma$	6.079, 4.234, 14.50	2.515	0.303
		6.044, 4.204, 14.43	2.516	0.261
Ca_3Cu	$Pm\bar{3}m$	5.099	2.113	0.280
		5.012	2.113	0.213
$MgCu_3$	$Pm\bar{3}m$	3.777	3.044	0.896
		3.767	3.048	0.976
$MgCu_2$	$Fd\bar{3}m$	7.074	2.972	0.834
		7.118	2.978	0.954
MgCu	$Pm\bar{3}m$	3.188	2.595	0.628
		3.194	2.594	0.698
Mg_2Cu	$Fddd$	9.179, 5.346, 18.59	2.291	0.564
		9.062, 5.283, 18.35	2.292	0.540

[a] Ref. 47.

nucleate and grow. Hence, the competing phase against the metallic glass is commonly a solid solution of a simple structure. Consequently, the information related to the glass formation can be obtained by comparing the relative stability of the solid solution with that of its amorphous counterpart.

Solid solution models are employed to compare the relative stability of the solid solution and its amorphous counterpart in this study. Then, the relevant Monte Carlo simulations[30] were performed as follows. Because the stable crystalline structures of Ca, Mg, and Cu are fcc, hcp, and fcc, respectively, two types of solid solution models, *i.e.* the hcp and fcc solid solution models, were established in the present study. For the fcc models, the [100], [010], and [001] crystalline directions are parallel to the x, y, and z axes, respectively, whereas for the hcp model, the [100], [001], and [120] crystalline directions are parallel to the x, y, and z axes, respectively. Periodic boundary conditions were applied in the three Cartesian directions. The fcc and hcp solid solution models consist of 2916 ($9 \times 9 \times 9 \times 4$) atoms and 2912 ($13 \times 8 \times 7 \times 4$) atoms, respectively. For a solid solution of $Ca_xMg_yCu_{1-x-y}$, the value of x and y varied with a composition interval of 5% to cover the range from 0 to 100%; thus, a thorough investigation on the entire compositional phase-space was carried out. While constructing the solid solution models, the solvent atoms were randomly substituted by a certain number of solute atoms to obtain the desired composition. The initial solid solutions were annealed at zero pressure and 300 K in an isothermal–isobaric ensemble.

3.1 Glass formation region for the Ca–Mg–Cu system

After sufficient simulation time, the initially constructed solid solution models either retain the initial crystalline state or collapse into a disordered state. Taking the $Mg_{20}Cu_{80}$ and $Ca_{40}Mg_{25}Cu_{35}$ alloys as examples, Fig. 2 shows the total pair-correlation functions $g(r)$ and atomic position projections of the two alloys. In Fig. 2(a), the $g(r)$ curve of $Mg_{20}Cu_{80}$ shows crystalline peaks, and in Fig. 2(c), the atoms are regularly arranged; this suggests a long-range ordered state. For $Ca_{40}Mg_{25}Cu_{35}$, as seen in Fig. 2(b), all the peaks beyond the second peak disappeared, exhibiting a feature of long range disorder and short-range order. This also corresponds to the result shown in Fig. 2(d) indicating that the crystalline lattice has collapsed into an amorphous state.

According to the $g(r)$ and atomic position projections, we performed the simulations over the entire Ca–Mg–Cu

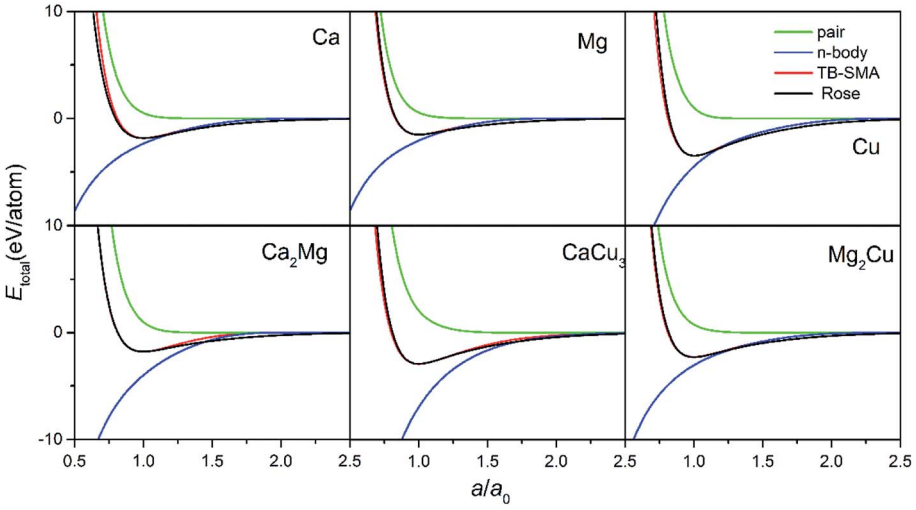

Fig. 1 Total energies, pair terms and n-body parts as a function of lattice constant calculated from the interatomic potential and Rose equation for Ca, Mg, Cu, Ca_2Mg, $CaCu_3$ and Mg_2Cu.

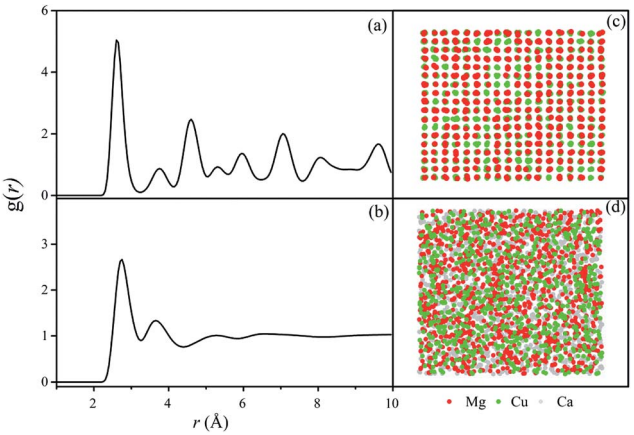

Fig. 2 Total pair-correlation functions $g(r)$ and atomic position projections of the $Mg_{20}Cu_{80}$ solid solution (a and c) and $Ca_{40}Mg_{25}Cu_{35}$ amorphous alloy (b and d). Red dots are for Mg, green dots are for Cu and gray dots are for Ca.

composition, and the result is shown in Fig. 3. The composition triangle was divided into four regions by three critical solubility lines. When an alloy composition locates beyond the lines AB, CD, EF, and moving towards one of the three corners, the crystalline structure remains stable and its formation is favored. These regions are, therefore, classified as crystalline regions. When the composition falls into the central hexagonal region enclosed by ABCDEF, the crystalline structure becomes unstable and spontaneously collapses into a disordered state. This hexagonal region is thus defined as the GFR. To validate the predicted GFR for the Ca–Mg–Cu system, experimental data was extensively obtained, as shown in Fig. 3 with the red dots.[15,31–36] It can be clearly seen that these experimental results mostly fall within the predicted hexagonal region; this suggests that our simulation scheme is quite reasonable for the Ca–Mg–Cu system.

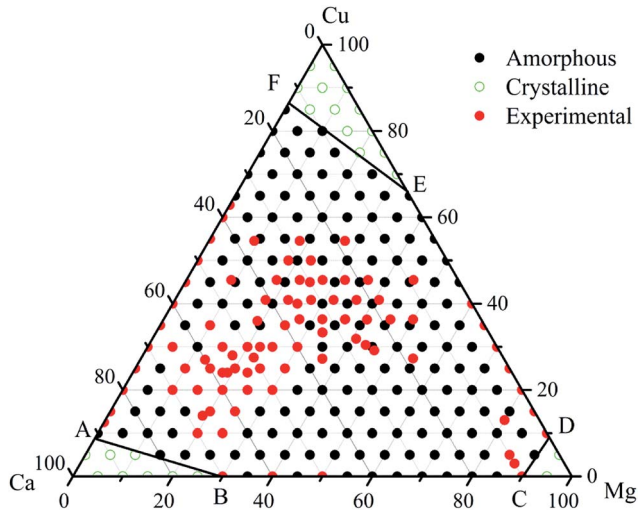

Fig. 3 Glass formation range of the Ca–Mg–Cu ternary system at 300 K derived from MC simulations.

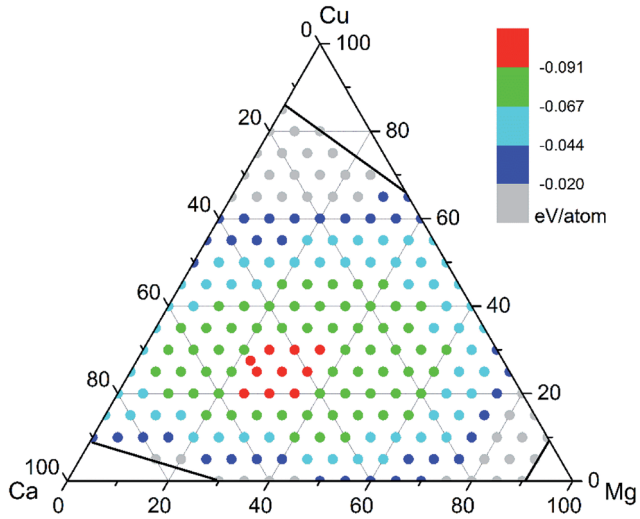

Fig. 4 Amorphous driving force of glass formation in the Ca–Mg–Cu ternary system at 300 K derived from MC simulations.

3.2 Composition optimization for glass formation

While seeking a reliable indicator to reflect the glass forming ability for a given system, amorphization driving force (ADF) for glass formation was revealed to be a promising criterion. To depict the amorphous driving force, the energy differences between the amorphous phase and solid solutions of each $Ca_xMg_yCu_{1-x-y}$, ΔE^{am}, were calculated as follows:

$$\Delta E^{am} = E_{am} - [xE_{Ca} + yE_{Mg} + (1 - x - y)E_{Cu}] \quad (4)$$

where E_{am} is the energy per atom of the $Ca_xMg_yCu_{1-x-y}$ amorphous phase and E_{Ca}, E_{Mg}, and E_{Cu} are the lattice energies of Ca, Mg, and Cu, respectively. Based on the calculation results, the contour map of the ADF within the GFR was plotted, as shown in Fig. 4. It can be seen that the compositions in the sub-region marked by the red dots promote a prominently larger ADF than those in the other regions; this suggests that the alloys in that sub-region more readily form metallic glasses and thus have a relatively larger GFA. Moreover, the results are well consistent with the experimental observations indicating that the better glass formers $Ca_{50}Mg_{25}Cu_{25}$ and $Ca_{50}Mg_{22.5}Cu_{27.5}$ have the maximum diameters of up to 9 mm and 10 mm,[15] respectively, whereas in other compositions with a lower ADF, such as $Ca_{27.3}Mg_{18.2}Cu_{54.5}$, the maximum diameter is around 1 mm.[35] Thus, the relevance of the optimal compositions of the Ca–Mg–Cu system as well as the validity of the constructed interatomic potential have been further confirmed.

IV. Characterization of the short-to medium-range order

Generally, glass formation as well as the properties of the resultant metallic glasses are closely related to the atomic-level structure, or specifically, to the short and medium-range orders in the metallic glasses.[37,38] In this section, we have elucidated the structural characteristics of the $Ca_{50}Mg_{25}Cu_{25}$ metallic glass

in the favored sub-region to shed light on its structural origin, particularly the modulation from the short- to medium-range order. The short-range order (SRO) is analyzed as a preliminary step using the Voronoi tessellation method,[39–41] which is widely used to characterize the local environments in the amorphous phase. While counting the coordination number (CN), the small cell faces smaller than 5% of the average face area of the Voronoi polyhedra were neglected. Moreover, to quantify the local structures of the metallic glasses, the SRO was also analyzed using the Honeycutt–Andersen (H–A) pair analysis,[42] which was based on the result of the Voronoi tessellation method.

Fig. 5 shows the spectrum of the CN around the Ca, Mg, and Cu atoms in $Ca_{50}Mg_{25}Cu_{25}$. It can be seen that the CNs are well-distributed over a quite wide range, with the most frequent CN = 9 and 10 for the Cu-centered clusters, CN = 12 and 13 for the Mg-centered clusters, and CN = 14 and 15 for the Ca-centered clusters. The observed correlation can be understood in terms of the atomic size difference. The Goldschmidt atomic radii of Ca, Mg, and Cu are 1.97, 1.60, and 1.25 Å, respectively.[24] The relatively larger atomic size of Ca permits more atoms in the nearest-neighboring shells and leads to a larger CN, followed by that for Mg and then Cu. The dense clustering of small-sized and large-sized clusters would lead to the efficient filling of space and enhancement in stability.

Moreover, the results of the H–A pair analysis on the local structures in the $Ca_{50}Mg_{25}Cu_{25}$ metallic glass are shown in Fig. 6. The 1551 index, which is considered as a characteristic of icosahedral ordering, the 1441 and 1661 indices, representative of the bcc ordering, the 1541 and 1431 indices, characteristic of distorted icosahedral ordering, and the 1421 and 1422 indices, representative of fcc ordering and hcp ordering, respectively, are presented. It is clearly seen that the local configurations in $Ca_{50}Mg_{25}Cu_{25}$ are dominated by the 1551 bond pairs; this indicates that motivated by the polytetrahedral packing principle,[41] the five-fold bonds and triangulated faces are indeed favored in the metallic glasses. Moreover, the local five-fold symmetry is essentially incompatible with the global crystallographic symmetry and thus can frustrate crystallization and consolidate the stability of the glassy alloy. Moreover, the distorted five-fold bond pairs with the indices of 1541 and 1431 also cover a large fraction of ~28%; this indicates that the geometrical construction of $Ca_{50}Mg_{25}Cu_{25}$ is distorted to some extent while accommodating multiple types of constituent atoms with diverse atomic sizes and chemical interactions. Moreover, a large number of crystalline-like bond pairs, especially bcc-like bond pairs, with the indices of 1661 and 1441 are also found in the local structure of the $Ca_{50}Mg_{25}Cu_{25}$ metallic glass; this suggests a local order more complex than the icosahedral-like alone. These four-fold and six-fold bipyramids can be considered to be rotational defects, *i.e.*, disclinations,[43] in metallic glasses, which are analogous to translational defects, *i.e.*, dislocations, in conventional crystals.[44] In addition, the fcc- or hcp-like bond pairs with the indices of 1421 and 1422 cover a relatively minor fraction. This phenomenon can be driven by the tendency of the systems to minimize energy since the fcc or hcp arrangements are shown to have smaller binding energies than that of the icosahedral order.[45] Thus, it is indicated that the local structure in $Ca_{50}Mg_{25}Cu_{25}$ embodies characters of both icosahedral- and bcc-like configurations.

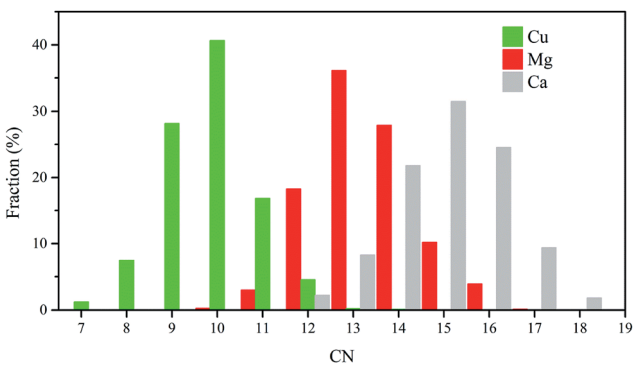

Fig. 5 Spectrum of CN around the Ca, Mg, and Cu atoms in $Ca_{50}Mg_{25}Cu_{25}$.

Based on the abovementioned analyses, we proceeded to interpret the characteristics in the medium-range order. Since the 1551 bond pairs, *i.e.*, pentagonal bipyramids, are the dominant SRO motifs in $Ca_{50}Mg_{25}Cu_{25}$, their connection mode and the resultant packing in space stands out as a plausible interpretation of MRO. To illustrate the network formed among these local clusters, a typical patch was extracted from the glassy matrix of $Ca_{50}Mg_{25}Cu_{25}$, as exhibited in Fig. 7. To illustrate the clustering of the local five-fold SRO motifs, only the 1551 bond pairs and associated pentagonal rings are displayed. It can be seen that string-like chains and networks are formed by the pentagonal bipyramids, which serve as the skeleton or backbone of the amorphous structure. Since the local five-fold symmetry renders the local environments incompatible for the formation of more crystalline-like symmetry, mutual interconnection among the five-fold motif will be encouraged, exhibiting some sense of cooperativity.[46] The extension of five-fold symmetry from the short-range to the medium-range and beyond appears to be a striking feature in many categories of metallic glasses,[47,48] and this cooperativity further facilitates the consolidation of the stability of metallic glasses.

To characterize the aggregation feature of the five-fold motif in $Ca_{50}Mg_{25}Cu_{25}$, the number of 1551 pairs in which each specific atom participates was statistically analyzed, as presented in the inset of Fig. 6(b). Most atoms in $Ca_{50}Mg_{25}Cu_{25}$ participate in the formation of two to eight 1551 bond pairs, with an average of ~4.98. Moreover, it is worth noting that only a small fraction, ~1.68%, of the atoms have twelve 1551 bond pairs around them, *i.e.*, exactly forming the icosahedra.[49] This is in contradiction to the long-held understanding that the five-fold pairs are a direct indication of icosahedral ordering. Similar to the Ca–Mg–Zn BMGS,[40] the Ca–Mg–Cu metallic glasses also proved that the system contained a very low fraction of icosahedra despite the observation that five-coordinated vertices dominated in all clusters.[50] By definition, in the H–A analysis, the individual bond pairs are considered to be basic structural motifs, whereas analysis of the coordination clusters, such as Voronoi tessellation analysis, actually considers all the

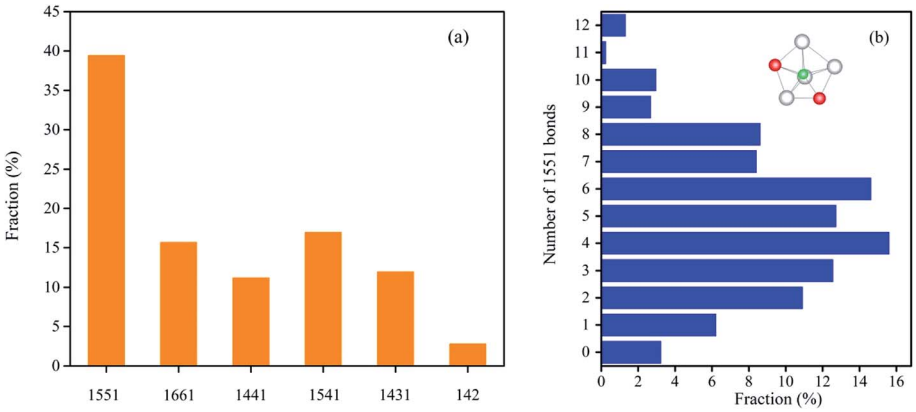

Fig. 6 (a) Percentage of local bond pairs, *i.e.* 1551, 1661, 1441, 1541, 1431, and 142 (abbreviation of 1421 and 1422) in the $Ca_{50}Mg_{25}Cu_{25}$ metallic glass. (b) Distribution of the number of 1551 pairs in each specific atom in the $Ca_{50}Mg_{25}Cu_{25}$ metallic glass.

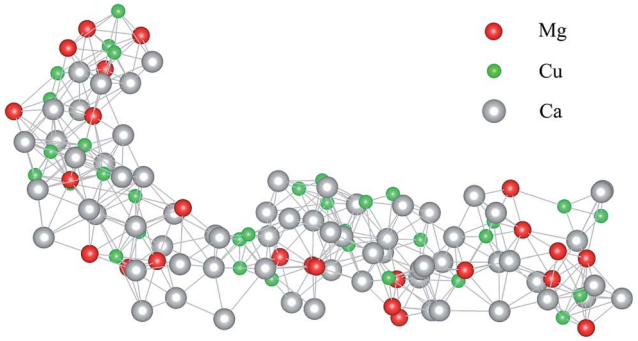

Fig. 7 A typical network extracted from the glassy matrix of $Ca_{50}Mg_{25}Cu_{25}$ to illustrate the clustering of the local fivefold SRO motifs. Only the 1551 bond pairs and the associated pentagonal rings are shown herein.

bond pairs in which a center atom is involved and offers a more complete description of the geometrical construction. Accordingly, it can be speculated that even with a given set of bond pairs, their combination mode, which can be reflected by the distribution of the coordination clusters, can vary significantly. In the present study, although icosahedra are not the predominant clusters in $Ca_{50}Mg_{25}Cu_{25}$, fragmented pentagonal bipyramids are still populated in the glassy matrix, just not exactly aggregating into the icosahedra. Due to the non-space filling nature of the five-fold symmetry, the disclination lines formed by the 1441 and 1661 bond pairs were dissolved in the extended network of the pentagonal bipyramids to occupy the voids and relieve the packing frustration. Therefore, a microscopic picture of the medium-range packing in Ca–Mg–Cu metallic glasses can be described as an extended network of pentagonal bipyramids entangled with four-fold and six-fold disclinations.

V. Conclusion

In conclusion, the glass formation range and ability of ternary Ca–Mg–Cu metallic glass are obtained *via* the atomistic approach. A realistic interatomic potential was first constructed for the Ca–Mg–Cu system based on the TB-SMA and then applied to Monte Carlo simulations to predict the favored composition for metallic glass formation. The simulation not only predicted a hexagonal composition region, within which Ca–Mg–Cu metallic glass formation was energetically favored, but also pinpointed the favored sub-region within which the amorphization driving force was larger than that outside. The GFA has a positive correlation with the critical size of the obtainable metallic glasses, which supports the prediction scheme and the relevance of our constructed potential. Further structural analysis indicates that the 1551 bond pairs (icosahedral-like) dominate in the $Ca_{50}Mg_{25}Cu_{25}$ metallic glass within the favored sub-region, which frustrate crystallization and consolidate the stability of the glassy phase. The large atomic size difference between Ca, Mg, and Cu extends the short-range landscape, and a microscopic picture of the medium-range packing can be described as an extended network of pentagonal bipyramids entangled with four-fold and six-fold disclinations, which together fulfill the space of the metallic glasses. The predictions are well supported by the experimental observations reported to date and can provide guidance for the design of ternary glasses.

Acknowledgements

The authors are grateful to the financial support received from the National Natural Science Foundation of China (51571129, 51631005), the Ministry of Science and Technology of China (2017YFB0702201, 2017YFB0702301, 2017YFB0702401), and the Administration of Tsinghua University.

References

1 J. J. Gilman, *J. Appl. Phys.*, 1975, **46**, 1435–1436.
2 W. Klement, R. H. Willens and P. Duwez, *Nature*, 1960, **187**, 869–870.
3 A. L. Greer and M. F. Ashby, *Scr. Mater.*, 2006, **54**, 321–326.

4 T. Lin, C. Yong-Qiang, S. Zhi-Wei, L. Ju, W. Cheng-Cai, H. Xiao-Dong, S. Jun and M. Evan, *Nat. Commun.*, 2012, **3**, 609.
5 J. Schroers, *Adv. Mater.*, 2010, **22**, 1566–1597.
6 W. H. Wang, C. Dong and C. H. Shek, *Mater. Sci. Eng., R*, 2004, **44**, 45–89.
7 B. A. Sun and W. H. Wang, *Prog. Mater. Sci.*, 2015, **74**, 211–307.
8 D. Turnbull, *Trans. Metall. Soc. AIME*, 1961, **221**, 422–439.
9 T. Egami and Y. Waseda, *J. Non-Cryst. Solids*, 1984, **64**, 113–134.
10 J. H. Li, X. D. Dai, S. H. Liang, K. P. Tai, Y. Kong and B. X. Liu, *Phys. Rep.*, 2008, **455**, 1–134.
11 D. Turnbull, *Contemp. Phys.*, 1969, **10**, 473–488.
12 A. Inoue, T. Zhang and T. Masumoto, *J. Non-Cryst. Solids*, 1993, **156**, 473–480.
13 Z. P. Lu and C. T. Liu, *Acta Mater.*, 2002, **50**, 3501–3512.
14 O. N. Senkov, D. B. Miracle and J. M. Scott, *Intermetallics*, 2006, **14**, 1055–1060.
15 O. N. Senkov, J. M. Scott and D. B. Miracle, *J. Alloys Compd.*, 2006, **424**, 394–399.
16 O. N. Senkov and J. M. Scott, *J. Non-Cryst. Solids*, 2005, **351**, 3087–3094.
17 V. Keppens, Z. Zhang, O. N. Senkov and D. B. Miracle, *Philos. Mag.*, 2007, **87**, 503–508.
18 O. N. Senkov, D. B. Miracle, V. Keppens and P. K. Liaw, *Metall. Mater. Trans. A*, 2008, **39**, 1888–1900.
19 O. N. Senkov and D. B. Miracle, *Metall. Mater. Trans. A*, 2010, **41**, 1677–1684.
20 J. H. Li, X. D. Dai, T. L. Wang and B. X. Liu, *J. Phys.: Condens. Matter*, 2007, **19**, 086228.
21 V. Rosato, M. Guillope and B. Legrand, *Philos. Mag. A*, 1989, **59**, 321–336.
22 D. Frenkel and B. Smit, *Understanding molecular simulation: From algorithms to applications*, Academic, New York, 2002.
23 M. D. Segall, P. J. D. Lindan, M. J. Probert, C. J. Pickard, P. J. Hasnip, S. J. Clark and M. C. Payne, *J. Phys.: Condens. Matter*, 2002, **14**, 2717–2744.
24 C. Kittel, *Introduction to Solid State Physics*, Wiley, New York, 2002.
25 D. R. Lide and T. J. Bruno, *CRC Handbook of Chemistry and Physics*, CRC Press, New York, 2002.
26 J. H. Rose, J. R. Smith, F. Guinea and J. Ferrante, *Phys. Rev. B: Condens. Matter Mater. Phys.*, 1984, **29**, 2963–2969.
27 B. X. Liu, W. S. Lai and Q. Zhang, *Mater. Sci. Eng., R*, 2000, **29**, 1–48.
28 J. M. Lopez, J. A. Alonso and L. J. Gallego, *Phys. Rev. B: Condens. Matter Mater. Phys.*, 1987, **36**, 3716–3722.
29 H. W. Sheng, G. Wilde and E. Ma, *Acta Mater.*, 2002, **50**, 475–488.
30 J. H. Li, S. Z. Zhao, Y. Dai, Y. Y. Cui and B. X. Liu, *J. Appl. Phys.*, 2011, **109**, 113538.
31 R. St. Amand and B. C. Giessen, *Scr. Metall.*, 1978, **12**, 1021–1026.
32 P. P. Mishra, M. Milanarun, N. Jha and A. K. Mishra, *J. Alloys Compd.*, 2002, **340**, 108–113.
33 F. Sommer, G. Bucher and B. Predel, *J. Phys.*, 1980, **41**(C8), C563–C568.
34 K. J. Laws, K. F. Shamlaye, J. D. Cao, J. P. Scicluna and M. Ferry, *J. Alloys Compd.*, 2012, **542**, 105–110.
35 K. J. Laws, K. F. Shamlaye, B. Gun and M. Ferry, *J. Alloys Compd.*, 2009, **486**, L27–L29.
36 K. Amiya and A. Inoue, *Mater. Trans.*, 2002, **43**, 81–84.
37 A. R. Yavari, *Nature*, 2006, **439**, 405–406.
38 H. R. Schober, *Phys. Chem. Chem. Phys.*, 2004, **6**, 3654–3658.
39 S. Y. Wang, M. J. Kramer, M. Xu, S. Wu, S. G. Hao, D. J. Sordelet, K. M. Ho and C. Z. Wang, *Phys. Rev. B: Condens. Matter Mater. Phys.*, 2009, **79**, 144205.
40 O. N. Senkov, D. B. Miracle, E. R. Barney, A. C. Hannon, Y. Q. Cheng and E. Ma, *Phys. Rev. B: Condens. Matter Mater. Phys.*, 2010, **82**, 104206.
41 H. W. Sheng, W. K. Luo, F. M. Alamgir, J. M. Bai and E. Ma, *Nature*, 2006, **439**, 419–425.
42 J. D. Honeycutt and H. C. Andersen, *J. Phys. Chem.*, 1987, **91**, 4950–4963.
43 D. R. Nelson, *Phys. Rev. B: Condens. Matter Mater. Phys.*, 1983, **28**, 5515–5535.
44 Y. Q. Cheng and E. Ma, *Prog. Mater. Sci.*, 2011, **56**, 379–473.
45 F. C. Frank, *Proc. R. Soc. London, Ser. A*, 1952, **215**, 43–46.
46 J. G. Kang, J. Y. Zhu, S. H. Wei, E. Schwegler and Y. H. Kim, *Phys. Rev. Lett.*, 2012, **108**, 115901.
47 Q. Wang, J. H. Li, J. B. Liu and B. X. Liu, *Phys. Chem. Chem. Phys.*, 2014, **16**, 19590–19601.
48 M. Lee, C.-M. Lee, K.-R. Lee, E. Ma and J.-C. Lee, *Acta Mater.*, 2011, **59**, 159–170.
49 J. Ding, Y. Cheng and E. Ma, *Acta Mater.*, 2013, **61**, 3130–3140.
50 O. N. Senkov, Y. Q. Cheng, D. B. Miracle, E. R. Barney, A. C. Hannon and C. F. Woodward, *J. Appl. Phys.*, 2012, **111**, 123515.